7-26-2017

Crystal structure, homogeneity range and electronic structure of rhombohedral γ-Mn5Al8

Srinivasa Thimmaiah
Ames Laboratory

Zachary Tener
Iowa State University

Tej N. Lamichhane
Iowa State University and Ames Laboratory, tejl@iastate.edu

Paul C. Canfield
Iowa State University and Ames Laboratory, canfield@ameslab.gov

Gordon J. Miller
Iowa State University and Ames Laboratory, gmiller@iastate.edu

Crystal structure, homogeneity range and electronic structure of rhombohedral γ-Mn5Al8

Abstract

The γ-region of the Mn–Al phase diagram between 45 and 70 at.% Al was re-investigated by a combination of powder and single crystal X-ray diffraction as well as EDS analysis to establish the distribution of Mn and Al atoms. Single crystals of γ-Mn5–*x* Al8+*x* were grown using Sn-flux at 650 °C. The crystal structure, atomic coordinates and site occupancy parameters of γ-Mn5–*x* Al8+*x* phases were refined from single crystal X-ray data. The γ-Mn5-*x* Al8+*x* phase adopts the rhombohedral Cr5Al8-type structure rather than a cubic γ-brass structure. The refined compositions from two crystals extracted from the Al-rich and Mn-rich sides are, respectively, Mn4.76Al8.24(2) **(I)** and Mn6.32Al6.68(2) **(II)**. The structure was refined in the acentric *R*3*m* space group (No.160, Z=6), in order to compare with other reported rhombohedral γ-brasses. In addition, according to X-ray powder diffraction analysis, at the Al-rich side the γ-phase coexists with LT–Mn4Al11 and, at the Mn-rich side, with a hitherto unknown phase. The refined lattice parameters from powder patterns fall in the range *a*=12.6814(7)–12.6012(5) Å and *c*=7.9444(2)–7.9311(2) Å from Al-rich to Mn-rich loadings, and the corresponding rhombohedral angles distorted from a pseudo-cubic cell were found to be 89.1(1)°–88.9(1)°. Magnetic susceptibility and magnetization studies of Mn4.92Al8.08(2) are consistent with moment bearing Mn and suggest a spin glass state below 27 K. Tight-binding electronic structure calculations (LMTO-ASA with LSDA) showed that the calculated Fermi level for γ-"Mn5Al8" falls within a pseudogap of the density of states, a result which is in accordance with a Hume-Rothery stabilization mechanism γ-brass type phases.

Keywords

electronic structure, flux method, intermetallic phase, single crystal, X-ray diffraction

Disciplines

Biological and Chemical Physics | Chemistry | Inorganic Chemistry | Materials Chemistry

Comments

This article is published as Thimmaiah, Srinivasa, Zachary Tener, Tej N. Lamichhane, Paul C. Canfield, and Gordon J. Miller. "Crystal structure, homogeneity range and electronic structure of rhombohedral γ-Mn5Al8." *Zeitschrift für Kristallographie-Crystalline Materials* 232, no. 7-9 (2017): 601-610. doi: 10.1515/zkri-2017-0003. Posted with permission.

Srinivasa Thimmaiah*, Zachary Tener, Tej N. Lamichhane, Paul C. Canfield and Gordon J. Miller

Crystal structure, homogeneity range and electronic structure of rhombohedral γ-Mn_5Al_8

DOI 10.1515/zkri-2017-0003
Received January 6, 2017; accepted March 7, 2017; published online April 7, 2017

Abstract: The γ-region of the Mn–Al phase diagram between 45 and 70 at.% Al was re-investigated by a combination of powder and single crystal X-ray diffraction as well as EDS analysis to establish the distribution of Mn and Al atoms. Single crystals of γ-$Mn_{5-x}Al_{8+x}$ were grown using Sn-flux at 650 °C. The crystal structure, atomic coordinates and site occupancy parameters of γ-$Mn_{5-x}Al_{8+x}$ phases were refined from single crystal X-ray data. The γ-$Mn_{5-x}Al_{8+x}$ phase adopts the rhombohedral Cr_5Al_8-type structure rather than a cubic γ-brass structure. The refined compositions from two crystals extracted from the Al-rich and Mn-rich sides are, respectively, $Mn_{4.76}Al_{8.24(2)}$ **(I)** and $Mn_{6.32}Al_{6.68(2)}$ **(II)**. The structure was refined in the acentric *R*3*m* space group (No.160, Z = 6), in order to compare with other reported rhombohedral γ-brasses. In addition, according to X-ray powder diffraction analysis, at the Al-rich side the γ-phase coexists with LT–Mn_4Al_{11} and, at the Mn-rich side, with a hitherto unknown phase. The refined lattice parameters from powder patterns fall in the range a = 12.6814(7)–12.6012(5) Å and c = 7.9444(2)–7.9311(2) Å from Al-rich to Mn-rich loadings, and the corresponding rhombohedral angles distorted from a pseudo-cubic cell were found to be 89.1(1)°–88.9(1)°. Magnetic susceptibility and magnetization studies of $Mn_{4.92}Al_{8.08(2)}$ are consistent with moment bearing Mn and suggest a spin glass state below 27 K. Tight-binding electronic structure calculations (LMTO-ASA with LSDA) showed that the calculated Fermi level for γ-"Mn_5Al_8" falls within a pseudogap of the density of states, a result which is in accordance with a Hume-Rothery stabilization mechanism γ-brass type phases.

Keywords: electronic structure; flux method; intermetallic phase; single crystal; X-ray diffraction.

Introduction

Structurally complex intermetallic compounds that are frequently observed in many binary [1–3] and ternary systems [4–7] consist of very large unit cells containing hundreds to thousands of atoms. They pose significant challenges for rationalizing the origin of complexity and understanding their crystal structures and factors governing their stability. Few generalized approaches have been developed to understand the stability of certain groups of intermetallic compounds such as Laves phases [8–12], Zintl phases [13–15] and Hume-Rothery phases [16]. For instance, the stability of Laves phases is rationalized based upon geometrical and electronic factors such as atomic size ratios, packing densities, electronegativity, and valence electron concentration (*vec*) or e^-/a ratio. For Hume-Rothery phases, which include structurally complex compounds such as γ-brasses, quasicrystals and their approximants, the stability and emergence of particular types of structures are mainly governed by e^-/a ratios (*vec*). For example, γ-brass and related structures emerge for *vec* of 1.54–1.75 e^-/a [17–21], whereas icosahedral quasicrystals and their crystalline approximant phases emerge at higher *vec*, of 1.75–2.10 e^-/a, depending upon the type of approximant [22, 23]. For both cases, the stability of these phases can be rationalized by the formation of a pseudogap at the Fermi level in the electronic density of states arising from interactions between the Fermi surface and Brillouin zone planes [22, 24, 25].

We have recently investigated the γ-phase regions of several binary *T*-Zn (*T* = Fe [26], Co [27], Pd [28] and Au [19]), *T*-Ga (*T* = Cr, Mn, and Fe) [29] and ternary *T*-Pd-Zn (*T* = Fe, Co, and Au) [17, 26, 27] and Pd–Al–Zn [18, 30] systems to gain better understanding of the relationships among chemical compositions, *vec*, structure stability, electronic structures, and magnetic properties. We have

***Corresponding author: Srinivasa Thimmaiah,** The Ames Laboratory, US Department of Energy, Iowa State University, Ames, Iowa 50011, USA, E-mail: srini@iastate.edu
Zachary Tener: Department of Chemistry, Iowa State University, Ames, Iowa 50011, USA
Tej N. Lamichhane and Paul C. Canfield: The Ames Laboratory, US Department of Energy, Iowa State University, Ames, Iowa 50011, USA; and Department of Physics and Astronomy, Iowa State University, Ames, Iowa 50011, USA
Gordon J. Miller: The Ames Laboratory, US Department of Energy, Iowa State University, Ames, Iowa 50011, USA; and Department of Chemistry, Iowa State University, Ames, Iowa 50011, USA

observed the formation of cubic γ-phases (*cI*52) for most of the binary and ternary systems, except for *T*-Ga [29], Au–Zn [19], Pd–Au–Zn [17] and Pd–Al–Zn [18] systems. The Pd–Au–Zn and Pd–Al–Zn systems revealed the presence of a γ-phase and as well $2\times2\times2$ superstructures denoted as γ′, *cF*400-*cF*416, depending upon *vec*. These γ′-phases stabilize at somewhat higher *vec* values compared to γ-phases in the same system and are associated with structural disorder and ordered vacancies at specific sites [17, 18]. The *vec* range observed for Pd–Zn–Al and Pd–Au–Zn systems was found to be 1.71–1.75 e^-/a and 1.63–1.65 e^-/a, respectively. On the other hand, rhombohedral γ-Au_5Zn_8 (*hR*78) was observed in the Au–Zn system with a noticeable phase width of 60–66 at.% Zn, which corresponds to a *vec* range of 1.61–1.66 e^-/a. Interestingly, γ-Au_5Zn_8 phases show additional nonstoichiometric vacancies on the outer tetrahedra (OT) and octahedra (OH) of 26-atom clusters apart from the ordered vacancies present at the center of each cluster. These nonstoichiometric vacancies play a decisive role in lowering the overall *vec* of the phase to the optimal values of ca. 1.615 e^-/a because the vacancy is treated as an atomic site with 0 valence electrons. As a part of our ongoing effort to understand the relationship between *vec* and vacancy concentration and ordering on the structural stability of γ-phases, we have investigated γ-Mn_5Al_8, which is reported to be rhombohedral with a noticeable phase width [31, 32].

A comprehensive experimental Mn–Al phase diagram was reported by Gödecke and Köster [33]. According to their report, the γ-phase region is assigned between 52 and 68 at.% Al, and consists of three different phases, namely γ, γ1 and γ2. According to this diagram, the room temperature γ2-phase displays two high temperature modifications, γ1 and γ. Later, the γ2-phase was reported to have composition Mn_5Al_8, and to adopt the rhombohedral Cr_5Al_8-type structure [31, 32]. Mn_5Al_8 forms as a result of a peritectoid reaction at 988 °C between high temperature MnAl(γ) and γ1. The structure of the γ1 phase is still unknown, whereas MnAl(h) adopts the W-type structure, as reported by Ellner [31]. In addition, the composition and homogeneity range of γ-Mn_5Al_8 was re-determined via powder X-ray diffraction and metallographic investigation. According to this report, the (reversible) phase transformation between MnAl(h) and RT-Mn_5Al_8 is a displacive transformation mediated through vacancies that give rise to a shear-like morphology as observed in SEM micrographs [31–33]. Furthermore, the high temperature MnAl(h) phase cannot be retained by quenching. A similar shear-like crystal morphology was also observed during the current studies when we obtained γ-Mn_5Al_8 through arc-melting, which resulted in mediocre quality crystals for single crystal diffraction analysis due to twinning (see Results and discussion). Hence, we employed a Sn-flux for growing crystals of γ-Mn_5Al_8 for single crystal diffraction experiments.

Although the structure of γ-Mn_5Al_8 was reported to be Cr_5Al_8-type, details of atomic arrangements and distribution of elements for structures within the homogeneity range have never been reported. In addition, our structural analysis of rhombohedrally distorted γ-Au_5Zn_8, which is also isostructural, revealed the presence of non-stoichiometric vacancies. Therefore, a re-evaluation of the crystal structure using single crystal diffraction and details of elemental distributions was warranted for γ-Mn_5Al_8 in order to establish the possible role vacancies may have to stabilize its structure over the entire homogeneity range.

Experimental

Synthesis and analysis

We have employed the Sn-flux method to grow a series of single crystals of γ- $Mn_{5-x}Al_{8+x}$ phases. Stoichiometric amounts of Mn (99.99%, Material Preparation Center (MPC), Ames Laboratory) and Al (99.99% MPC, Ames Laboratory) were weighed according to the compositions, and Sn was added with a 1:4 molar ratio [($Mn_{5-x}Al_{8+x}$):Sn = 1:4]. The surface oxide layer on Mn was removed by etching with dilute HCl (5 M) followed by drying with acetone that resulted in a shiny surface. These targeted compositions were placed in alumina crucibles and then sealed in evacuated silica tubes under vacuum (10^{-5} torr). The tubes were heated continuously from ambient temperature to 800 °C at a heating rate 30 °C/h, and held there for 12 h. The reaction mixtures were then cooled to 650 °C at a cooling rate of 30 °C/h, at which point the samples were equilibrated for 4 days. The excess Sn (flux) was removed by centrifugation at 650 °C.

To check phase purity and assess the homogeneity range, all samples were examined by powder X-ray diffraction using a Philips PANalytical X′Pert PRO diffractometer. The samples were mounted on specially cut single crystal silicon and spread evenly with the aid of laboratory grade acetone. Data were collected for 2θ values ranging from 10° to 90° at increments of 0.02° via a continuous scan mode using Cu K_α radiation (λ = 1.540598 Å) in Bragg-Brentano geometry. All X-ray diffraction powder patterns showed the presence of a small amount of unreacted Sn-flux along with the desired phase. Lattice parameters were refined using the *WINXPOW* program [34].

Semiquantitative microprobe analyses were performed on several single crystals using a JEOL 5910LV scanning electron microscope equipped with a Noran-Vantage energy-dispersive spectrometer. To achieve more accurate compositions, samples were embedded in the epoxy and carefully polished to obtain a flat surface. The energy dispersive X-ray (EDS) spectra were acquired using an accelerating voltage of 20 keV. Images were also taken in the back-scattered electron mode to check for the presence of any additional phases. The chemical compositions obtained from EDS corroborate well with refinements from single crystal data analyses, within the limitations of the technique. No heavy elements other than Mn and Al were detected.

Single crystal structure determination

Several suitable single crystals from six different nominal compositions were selected to examine the phase width and the elemental distributions among the Mn–Al γ-phases. All crystals were studied using a Bruker APEX CCD diffractometer equipped with graphite-monochromatized Mo Kα radiation (λ = 0.71073 Å). Reflections were gathered at room temperature by taking three sets of 606 frames with 0.3° scans in ω, with an exposure time of 15–20 s per frame using the *APEX 2* program package [35]. The range of 2θ extended from 6 to 59°. The measured intensities were corrected for Lorentz and polarization effects, as well as for absorption using the program *SADABS*, as implemented in *APEX 2* program package [35]. All data sets showed the systematic absence condition, *hkl:* $-h+k+l=3n$, etc., which suggests rhombohedral symmetry and five possible space groups, $R\bar{3}$, *R*3, *R*3*m*, *R*32, and $R\bar{3}m$. Although the *E*-Stats model strongly suggested the structures to be centrosymmetric, space group $R\bar{3}m$, all structures were refined in the non-centrosymmetric space group *R*3*m* to establish structural relationships to the known rhombohedrally distorted γ-brass type structures. No significant differences in compositions were observed between refinements in *R*3*m* and $R\bar{3}m$. The single crystal refinements for $R\bar{3}m$ are presented in Supporting Information for comparison. Herein, we report detailed structural refinements of two specimens: one extracted from an Al-rich (**I**: $Mn_{3.9}Al_{9.1}$, loaded composition, co-existing with Mn_4Al_{11}) and the other from a Mn-rich (**II**: $Mn_{7.15}Al_{5.85}$, loaded composition, co-existing with an unknown phase) sample. The refined compositions of the remaining crystals fall between these two extremes, and some of these results are summarized in Table 4.

Structure refinements

The atomic positions for crystal **I**, extracted from the Al-rich side and co-existing with Mn_4Al_{11}, were determined using direct methods as implemented in SHELXTL [36], which yielded nine crystallographic positions, three of which assigned as Mn and the rest as Al atoms. Subsequent isotropic least-squares refinement cycles converged quickly to R1 = 8.4%. The displacement parameters of two Al positions showed negative (M2 and M7) and another Al position (M6) showed relatively small values, which suggested possible Mn/Al mixing on these three sites. Possible inclusion of Sn on these positions was ruled out because EDS analyses revealed only the presence of Mn and Al in these crystals. In subsequent refinement cycles, these positions were assigned as mixtures of Mn and Al, the result of which dropped the *R*-value to 3%. At this stage, to ensure accurate compositions, the site occupancy parameters of all other positions (Al1, Mn3-Mn5, Al8 and Al9) were refined in a separate series of least-squares cycles, and yielded full occupancies within three standard deviations. The final stages of refinements were carried out including anisotropic displacement parameters to give R1 = 1.6% for 57 parameters. The refined composition was found to be $Mn_{4.76(1)}Al_{8.24}$, which agrees well with the EDS analysis (EDS = $Mn_{38(2)}Al_{62(2)} = Mn_{4.9}Al_{8.1}$).

The starting parameters of crystal **I** were used for the initial structure refinement of crystal **II**, which was extracted from the Mn-rich loaded composition "$Mn_{7.15}Zn_{5.85}$". According to our observed powder pattern, the γ-phase with nominal composition "$Mn_{7.15}Zn_{5.85}$" co-exists with an unknown phase. After a few cycles of isotropic refinement, the R1 value dropped to 3%. However, the Al1, Al8 and Al9 atoms showed relatively very small (almost negative) displacement parameters indicating possible mixing of Mn on their sites. In addition, freely refined occupancy parameters for Al1, Al8 and Al9 positions showed more than 100% occupancy to confirm the possible mixing of Mn on these sites. In the following refinement cycles, these positions were treated as mixed Al/Mn positions, and the Al occupancy on these sites refined to 90(1)%, 87(1)%, and 95(1)%, respectively, for Al1, Al8 and Al9. On the other hand, the occupancy parameter of the mixed Mn/Al (M6) position refined to 99(1)% Al, so this position was treated as fully occupied by Al. The final stage of refinements included anisotropic displacement parameters and yielded R1 = 1.9% for 59 parameters. The refined composition was found to be $Mn_{6.32(1)}Al_{6.68}$, which is also in good agreement with EDS analysis (EDS = $Mn_{48(2)}Al_{52(2)} = Mn_{6.2(2)}Al_{6.8(2)}$). Tables 1 and 2 summarize the atomic positions, site occupancy factors, and displacement parameters for crystals **I** and **II**.

Electronic structure calculations

The Stuttgart tight-binding, linear-muffin-tin orbital (TB-LMTO) [37–40] program with the atomic sphere approximation (ASA) was utilized to calculate the density of states (DOS) and crystal orbital

Tab. 1: Crystallographic data for crystals **I**, extracted from loaded composition $Mn_{35}Al_{65}$, and **II**, extracted from the loaded composition $Mn_{55}Al_{45}$.

	I	**II**
Empirical formula	$Mn_{4.76}Al_{8.24(2)}$	$Mn_{6.32}Al_{6.68(2)}$
Formula weight	483.69	527.49
Wavelength (Å)	0.71073	
Crystal system, space group	Rhombohedral, *R*3*m* (160)	
Unit cell dimensions, *a* (Å)	12.6740(4)	12.6012(5)
c	7.9461(3)	7.9311(3)
Volume (Å³); Z	1105.38(8); 6	1090.66(10); 6
Calculated density (g/cm³)	4.360	4.819
Absorption coefficient (mm^{-1})	8.820	11.344
Crystal size (mm^3)	0.11×0.08×0.05	0.15×0.08×0.06
θ range (°)	3.16–31.32	3.17–3.3
Limiting indices	$-17<=h<=18$, $-17<=k<=18$, $-10<=l<=10$	$-17<=h<=18$, $-18<=k<=18$, $-11<=l<=11$
Reflections collected / unique	5763/870 [R(int) = 0.0374]	5707/855 [R(int) = 0.0450]
Refinement method	$\|F\|^2$	
Data/parameters	870/57	855/59
Goodness-of-fit on $\|F\|^2$	1.047	1.023
Final R indices [$I > 2\sigma(I)$]	R1 = 0.0162 *w*R2 = 0.0304	R1 = 0.0187 *w*R2 = 0.0340
R indices (all data)	R1 = 0.0251 *w*R2 = 0.0332	R1 = 0.0292 *w*R2 = 0.0369
Extinction coefficient	0.00449(6)	0.00168(3)
Absolute structure parameter	0.46(5)	0.46(7)
Largest diff. peak and hole e · Å^{-3}	0.393 and −0.28	0.448 and −0.618

Tab. 2: Atomic coordinates and equivalent isotropic displacement parameters (Å²) for crystals **I** and ***II (bold italic)***.

	Atom	Wyck.	Occ. Al/Mn	*x*	*y*	*z*	U_{eq}
IT(1)	Al1	3*a*	1	0	0	0.1799(8)	0.008(1)
			0.86/0.14(1)	***0***	***0***	***0.1760(10)***	***0.007(1)***
IT(3)	M2	9*b*	0.49/0.51(1)	0.7404(1)	0.2596(1)	0.2607(1)	0.012(1)
			0.13/0.87(1)	***0.7386(1)***	***0.2614(1)***	***0.2615(1)***	***0.011(1)***
OT(1)	Mn3	3*a*	1	0	0	0.6773(5)	0.005(1)
			1	***0***	***0***	***0.6777(6)***	***0.005(1)***
OT(3)	Mn4	9*b*	1	0.5497(1)	0.4503(1)	0.4409(1)	0.006(1)
			1	***0.5501(1)***	***0.4499(1)***	***0.4395(1)***	***0.004(1)***
OH(3)	Mn5	9*b*	1	0.1173(1)	0.8827(1)	0.2471(1)	0.006(1)
			1	***0.1166(1)***	***0.8834(1)***	***0.2480(1)***	***0.007(1)***
OH(3′)	M6	9*b*	0.96/0.04(1)	0.5493(1)	0.4507(1)	0.0853(1)	0.008(1)
			1/0	***0.5502(1)***	***0.4498(1)***	***0.0863(1)***	***0.004(1)***
CO(3)	M7	9*b*	0.72/0.28(1)	0.2601(1)	0.7399(1)	0.0931(1)	0.002(1)
			0.33/0.67(1)	***0.2613(1)***	***0.7387(1)***	***0.0920(1)***	***0.002(1)***
CO(3′)	M8	9*b*	1/0	0.4502(1)	0.5497(1)	0.2698(1)	0.010(1)
			0.84/0.16(1)	***0.4502(1)***	***0.5497(1)***	***0.2712(1)***	***0.013(1)***
CO(6)	M9	18*c*	1/0	0.3348(1)	0.0441(1)	0.3418(4)	0.009(1)
			0.93/0.07(1)	***0.3329(1)***	***0.0460(1)***	***0.3435(6)***	***0.009(1)***

U(eq) is defined as one third of the trace of the orthogonalized Uij tensor.

Hamiltonian population (COHP) [41] curves for a rhombohedral structure of "Mn_5Al_8", as a hypothetical representative of the entire γ-phase region. Exchange and correlation were treated in the local density approximation [42]. All relativistic effects except spin-orbit coupling were taken into account by using the scalar relativistic approximation [43]. In the ASA, space is filled with small, overlapping Wigner-Seitz (WS) spheres at each atomic site. The symmetry of the potential is considered to be spherical inside each WS sphere, and a combined correction takes into account the overlapping part [44]. The radii of the WS spheres were obtained by requiring that the overlapping potential be the best possible approximation to the full potential, and were determined by an automatic procedure [44]. No empty spheres were required to satisfy the LMTO volume criterion. The corresponding WS radii for the various atoms include the following ranges: Mn, 2.813–2.862 Å; Al, 2.810–2.852 Å. The basis set included Mn 4*s*, 4*p*, and 3*d* orbitals, and Al 3*s* and 3*p* orbitals. The *k*-space integrations were accomplished by the tetrahedron method [45]. The self-consistent charge density was obtained by using 364 irreducible *k*-points in the Brillouin zone for the rhombohedral cell.

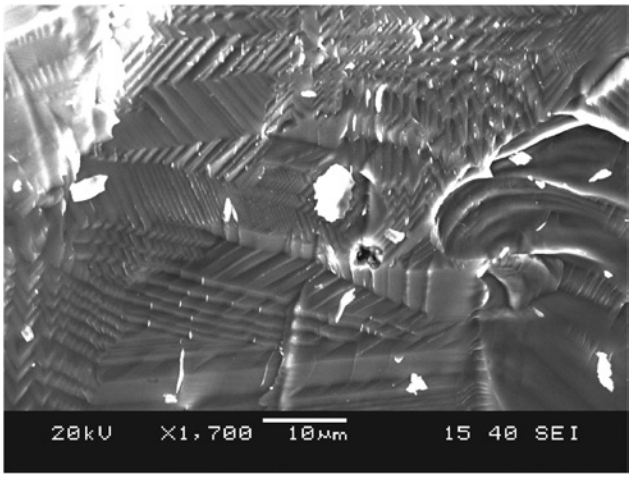

Fig. 1: SEM image of an arc melted sample with nominal composition "MnAl" after annealing at 700 °C for 5 days. A small amount of Mn evaporated during arc melting.

Results and discussion

Our exploration of the γ-region i.e. 45–70 at.% Al in the Mn–Al phase diagram *via* synthesis and crystallographic investigation revealed the existence of a rhombohedrally distorted γ-brass type phase. Single crystals suitable for single crystal diffraction analysis were successfully grown using a Sn-flux, whereas an arc melted sample with a nominal composition "MnAl" resulted in a single γ-type phase with a shear-like crystal morphology, as shown in Figure 1. The quality of single crystals for diffraction studies from arc melting followed by annealing at 700 °C were found to be mediocre. This could result from a displacive transformation from MnAl (h) to LT–Mn_5Al_8 mediated through constitutional vacancies [31]. The homogeneity range of the γ-phase established during this study agrees with earlier experimental results by Ellner [31], who investigated the γ-phase region of the Mn–Al phase diagram by powder X-ray diffraction and metallography. According to his report, the γ-phase adopts the rhombohedral Cr_5Al_8-type structure with a phase width of 52–63 at.% Al, but no atomic distributions of the constituent elements were

reported for any of the phases. Our recent comprehensive exploration of rhombohedrally distorted γ-brass phases $Au_{5-x}Zn_{8+y}$ revealed the presence of vacancies on certain crystallographic sites, an outcome that leads to favorable *vec* values to stabilize γ-brass type structures i.e. 1.61 and 1.66 e^-/atom [19]. We have also shown that the formation of additional stoichiometric and non-stoichiometric vacancies is critical to adjust the overall *vec* that stabilize superstructures of γ-brasses in Pd–Al–Zn [18] and Pd–Au–Zn [17] systems. Therefore, the absence of any structural information for rhombohedral γ- $Mn_{5-x}Al_{8+x}$ over its phase width motivated us to re-assess this phase and its structure.

Phase analysis

To estimate the phase width of the γ-region of the Mn–Al phase diagram, X-ray powder diffractograms (XRD) of various $Mn_{5-x}Al_{8+x}$ ($-2 \le x \le 1$ or ~45–70 at.% Al) samples were analyzed. Figure 2, shows the powder XRD patterns of various samples which were synthesized in a Sn-flux. Although all XRD patterns showed the presence of small amount of unreacted Sn in these samples, this did not interfere with the phase analysis nor single crystal diffraction studies. At the Al-rich side, i.e. for "Mn_4Al_9," the γ-phase co-exists with triclinic LT–Mn_4Al_{11} [46]. Single phase γ-brass was observed for a composition range between 50(2) and 62(2) at.% Al. On the other hand, at the Al-poor side, i.e. 45 at.% Al, the γ-phase co-exists with a hitherto unknown phase. Analysis of the powder XRD pattern of nominal composition "$Mn_{55}Al_{45}$" showed few additional peaks that could not be indexed with either a W- or CuAu-type structure. According to Ellner, at 957 °C, γ-Mn_5Al_8 transforms to MnAl(h), which adopts the W-type structure based on high-temperature X-ray diffraction studies. The high temperature MnAl(h) phase cannot be retained by quenching, although it transforms into Mn_5Al_8 (distorted γ-brass) upon cooling. This phase transformation is reversible which is mediated through displacement of atoms as well as the presence of constitutional vacancies [31]. The additional reflections also could not be indexed with a metastable τ-MnAl phase, which is stable up to 850 °C [47, 48]. τ-MnAl is ferromagnetic with a high Curie temperature of 382 °C and is a potential candidate for a rare-earth free permanent magnet [47, 49].

Lattice parameters, *a* and *c*, and unit cell volumes of the γ-type phase refined from X-ray powder patterns from several different nominal compositions are plotted vs. Al content in Figure 3. All values, except the *c*-axis parameter at higher Al content, increase monotonically as the Al

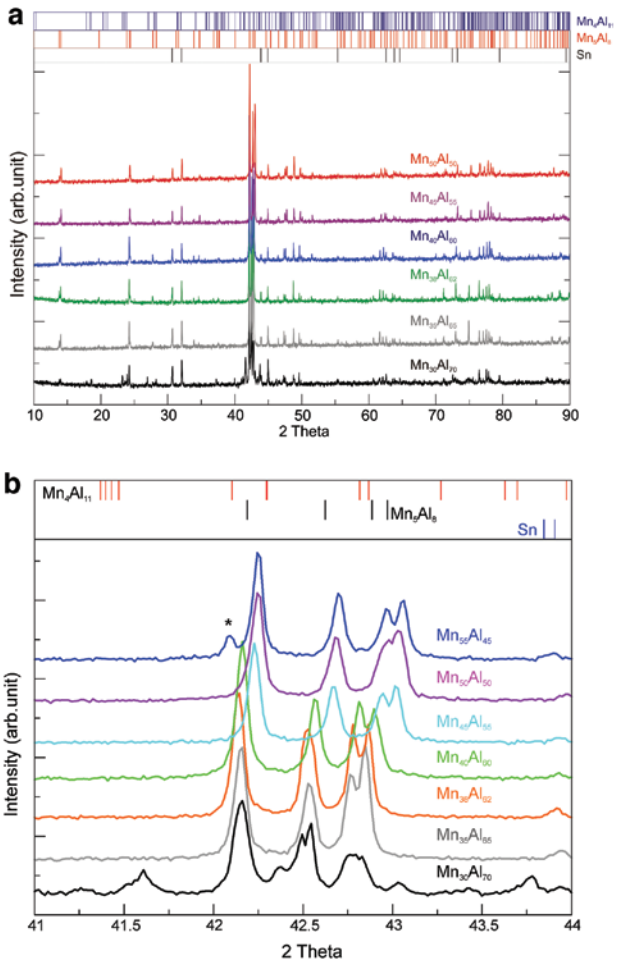

Fig. 2: Powder XRD patterns of various samples which were synthesized in a Sn-flux. (a) Powder X-ray diffraction patterns of Mn–Al mixtures (45–70 at.% Al) synthesized using a Sn-flux. (b) Expanded region, highlighting the splitting of main reflections due to rhombohedral distortion. The asterisk represents the additional reflection from an unknown phase.

content increases, a result that nicely corroborates with sizes of Mn and Al: the metallic radius of Al (1.432 Å for coordination #12) is significantly larger than that of Mn (1.272 Å for coordination #12) [50]. The refined cell volumes range from 1090.64(6) $Å^3$ (refined composition $Mn_{6.32(1)}Al_{6.68}$; ~51.3 at.% Al) to 1106.3(2) $Å^3$ (refined composition $Mn_{4.76(2)}Al_{8.24}$; ~63.3 at.% Al) for Mn-rich and Al-rich regions, respectively. A similar increase of unit cell volume with increasing Al content has been observed for rhombohedral γ-Cr_5Al_8 phases [51]. Furthermore, a noticeable variation in the *c*-axis value is observed mainly for Al-rich compositions. This is most likely due to overlapping reflections from triclinic LT–Mn_4Al_{11}, as seen in the Figure 2, that can affect accurate determination of lattice parameters. Nevertheless, these refined lattice parameters are in good agreement with the data presented by Ellner. Therefore, based on combined

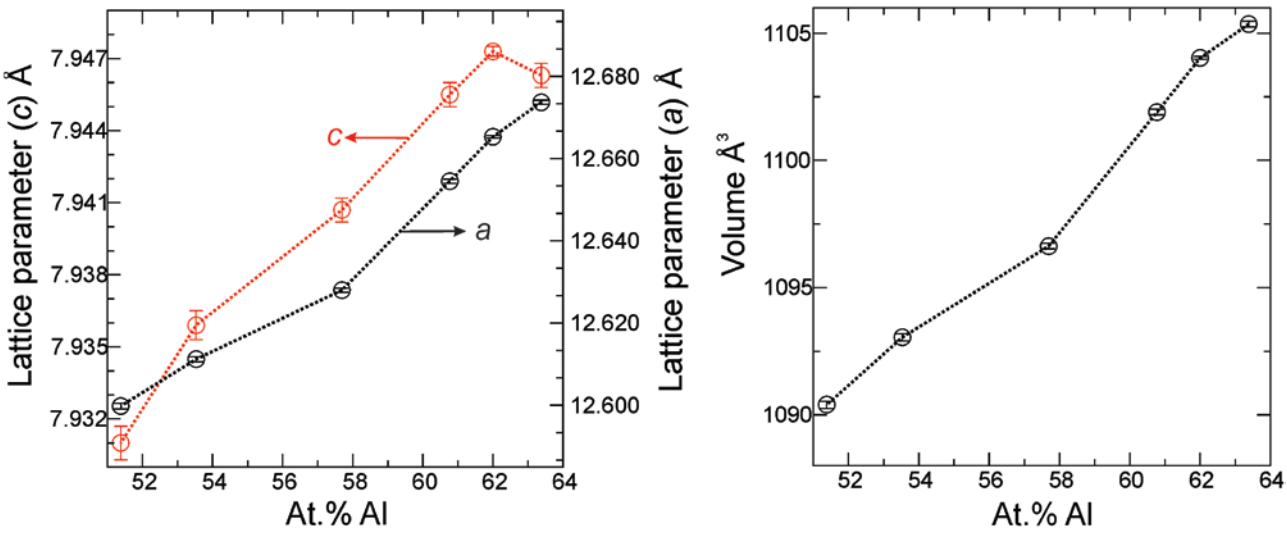

Fig. 3: Variation of lattice parameters (Å) and unit cell volume (Å³) as a function of Al content refined from PXRD patterns for γ-phases in the Mn–Al binary system.

single crystal diffraction and EDS studies, the upper and lower boundaries of the γ-type Mn–Al phase are assigned as 51.4–63.4 at.% Al at 650 °C.

As evident from the observed splitting of the main reflection in the PXRD patterns of Figure 2b, the rhombohedral distortion from cubic symmetry is significant. To evaluate the degree of distortion from cubic symmetry, we have determined the angles of the primitive rhombohedral cell from the refined lattice parameters and they range from 89.1(1)° to 88.9(1)°, respectively, for Al-rich to Al-poor regions. Most of the observed rhombohedrally distorted γ-brass type phases, such as *T*Ga (*T* = Cr, Mn and Fe), Au_5Zn_8, and Cr_5Al_8 show these angles to be less than 90°, except Cu_7Hg_6 which give 90.4° [52]. For γ-$Au_{5-x}Zn_{8+y}$ and γ-$Cr_{5\pm x}Al_{8\pm x}$ these angle ranges are 89.68–89.91° and 89.3–89.49°, respectively [19, 51]. Among 3*d* transition metal aluminides, the rhombohedrally distorted γ-brass type structure is observed for Cr_5Al_8 and Mn_5Al_8, whereas V_5Al_8 [53] and Fe_5Al_8 (HT-Phase) [54] are body-centered cubic structured.

Structural analysis

According to single crystal and powder diffraction studies, the γ-phase in the Mn–Al phase diagram adopts a distorted γ-Cr_5Al_8 type structure with a homogeneity range between 53.3(2) and 63.3(2) at.% Al at 650 °C. The structural refinements ware carried out for crystals **I** and **II** in the non-centrosymmetric space group *R*3*m* (*Z* = 6) extracted from the Al-rich ($Mn_{30}Al_{70}$) and Mn-rich ($Mn_{55}Al_{45}$) phase boundaries of the γ-region. The refined compositions of crystals **I** and **II** were found to be $Mn_{4.76(2)}Al_{8.24}$ and $Mn_{6.32(1)}Al_{6.68}$, respectively. In addition, refined compositions for other crystals that were extracted from different nominal compositions are tabulated in Table 3 along with R1 values. The site mixings in these crystals are similar to either crystal **I** or **II**. The atomic distributions of Mn and Al atoms on different sites of the 26-atom γ-cluster are given in Table 4.

The cubic γ-brass structure consists of two 26-atom γ-clusters, packed in a body-centered cubic fashion. Each γ-cluster can be decomposed into four successive polyhedral shells consisting of (i) an inner tetrahedron (IT) of four atoms; (ii) an outer tetrahedron (OT) of four atoms; (iii) an octahedron (OH) of six atoms; and (iv) a distorted cuboctahedron (CO) of 12 atoms. In cubic γ-brasses, these γ-clusters have $\bar{4}3m$ (T_d) symmetry. This structural description has been effectively used for numerous γ-, γ′-, and other distorted γ-brass phases, and has yielded exceptional insights about the structural chemistry and atomic distributions in γ-brasses, in general.

Tab. 3: Results from single crystal structural refinement for six different crystal extracted from different loaded compositions along with their corresponding residual R1/*w*R2 values and EDS results.

#	Loaded composition	Refined composition	R1/*w*R2	EDS results
I	$Mn_{35}Al_{65}$	$Mn_{4.76}Al_{8.24(2)}$	0.0162/0.0304	$Mn_{4.9(2)}Al_{8.1(2)}$
	$Mn_{38}Al_{62}$	$Mn_{4.92}Al_{8.08(2)}$	0.0219/0.0348	–
	$Mn_{40}Al_{60}$	$Mn_{5.10}Al_{7.90(2)}$	0.0296/0.0663	$Mn_{5.3(2)}Al_{7.7(2)}$
	$Mn_{45}Al_{55}$	$Mn_{5.50}Al_{7.50(2)}$	0.0181/0.0372	–
	$Mn_{50}Al_{40}$	$Mn_{6.04}Al_{6.96(2)}$	0.0197/0.0370	$Mn_{5.9(2)}Al_{7.1(2)}$
II	$Mn_{55}Al_{45}$	$Mn_{6.32}Al_{6.68(2)}$	0.0187/0.0340	$Mn_{6.2(2)}Al_{6.8(2)}$

Tab. 4: Atomic distributions, expressed as % Mn/% Al, on different sites of 26-atom γ-cluster refined from six different compositions listed in Table 4.

Composition	IT		OT		OH		CO		
	3*a* IT(1)	9*b* IT(3)	3*a* OT(1)	9*b* OT(3)	9*b* OH(3)	9*b* OH(3′)	9*b-I* CO(3)	9*b-II* CO(3′)	18*c* CO(6)
$Mn_{4.76}Al_{8.24(2)}$	0/100	51/49	100/0	100/0	100/0	04/96	28/72	0/100	0/100
$Mn_{4.92}Al_{8.08(2)}$	0/100	57/43	100/0	100/0	100/0	05/65	32/68	0/100	0/100
$Mn_{5.10}Al_{7.90(2)}$	0/100	59/41	100/0	100/0	100/0	08/92	39/61	0/100	0/100
$Mn_{5.50}Al_{7.50(2)}$	05/95	53/47	100/0	100/0	100/0	0/100	72/28	07/93	0/100
$Mn_{6.04}Al_{6.96(2)}$	10/90	76/24	100/0	100/0	100/0	0/100	67/33	13/87	05/95
$Mn_{6.32}Al_{6.68(2)}$	14/86	87/13	100/0	100/0	100/0	0/100	67/33	16/84	07/93

For rhombohedrally distorted γ-$Mn_{5-x}Al_{8+x}$, the γ-clusters adopt 3*m* (C_{3v}) symmetry, shown in Figure 4. For crystal **I** (Al-rich), the Al1 (3*a*) and M2 (9*b*) sites form the IT, surrounded by the OT of Mn3 (3*a*) and Mn4 (9*b*) sites. This is enclosed by an OH made up of 3 Mn5 (9*b*) and 3 M6 (9*b*) sites, and is further encased by a CO composed of 3 M7 (9*b*), 3 Al8 (9*b*), and 6 Al9 (18*c*) positions. This structural model (**I**) is very similar to that of γ-Cr_5Al_8 in terms of atomic distributions. A noticeable difference regarding Mn/Al mixing occurs for crystal **II**. The atomic positions that are completely occupied by Al in crystal **I** show some degree of mixing with Mn on Al1, Al8 and Al9 positions. On the other hand, the M6 site of the OH is fully occupied by Al for crystal **II** (Mn-rich). Over the entire homogeneity range, the OT position is occupied solely by Mn atoms, which is also true for γ-Cr_5Al_8, in which Cr atoms occupy the OT positions.

The major contributions to the phase width of γ-$Mn_{5-x}Al_{8+x}$ arises from changes in Mn:Al ratios on the IT (3*a*+9*b*) and CO (9*b*+9*b*+18*c*) sites of the 26-atom γ-cluster. The trends of increasing Mn occupancies on IT and CO sites are clearly visible with increasing Mn content in the structure. For the Al-rich region, a very small contribution from the OH site towards composition can also be seen, but these variations are negligible. The changes in chemical compositions and site occupancies of the 26-atom γ-cluster from different refinements are listed in Table 4. For instance, for the Al-rich γ-phase, the 3*a* IT position is completely occupied by Al, and nearly one-half of the 9*b* IT position is occupied by Mn, whereas 28% of Al has been replaced by Mn on one of the 9*b-I* CO sites, and the remaining 9*b-II* and 18*c* CO sites are occupied by Al. Therefore, the composition of the 26-atom γ-cluster of crystal **I** can be expressed as $(Al_{2.47}Mn_{1.53})^{IT}(Mn_4)^{OT}(Mn_{3.12}Al_{2.88})^{OH}(Al_{11.16}Mn_{0.84})^{CO}$. On the other hand, for the Al-poor side, 14% of the 3*a* IT position is occupied by Mn and there is further enrichment of Mn on the 9*b* IT site, from 51 to 87%. All three positions of the CO show mixed Mn/Al occupancies of 67, 16 and 7%, respectively, on 9b-*I*, 9*b-II*, and 18*c*. The chemical composition of the 26-atom γ-cluster for crystal **II** can be written as $(Al_{1.25}Mn_{2.75})^{IT}(Mn_4)^{OT}(Mn_3Al_3)^{OH}(Al_{9.1}Mn_{2.9})^{CO}$. The variation in chemical composition between crystals **I** and **II** is also reflected in noticeable changes in distances between different pairs of atoms. The most significant distance changes are observed for IT–IT and CO–CO contacts, because these atomic positions are mainly responsible for the phase width of γ- $Mn_{5-x}Al_{8+x}$. In particular, the Al1–M2 distances for crystals **I** and **II** are 2.578(5) Å and 2.516(6) Å, respectively; the Al9(M9)–Al9(M9) distances are 3.126(1) and 3.036(1) Å, respectively. Other noticeable changes in interatomic distances are presented in Supporting Information.

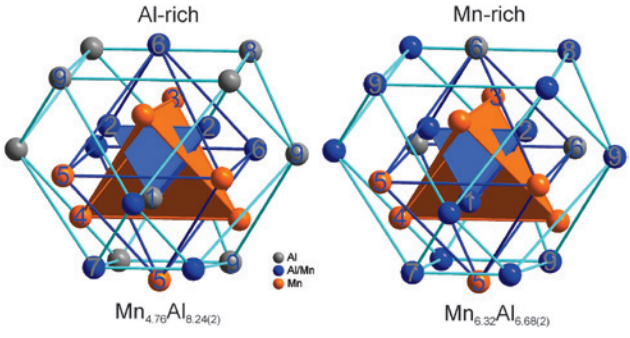

Fig. 4: The 26-atom cluster of γ-$Mn_{5-x}Al_{8+x}$ for Al-rich and Mn-rich (**I** and **II**), showing successive shells of atoms.

Single crystal structural refinements on several compositions revealed that no stoichiometric or non-stoichiometric vacancies occurs throughout the γ- $Mn_{5-x}Al_{8+x}$ series. In contrast, rhombohedrally distorted γ-$Au_{5-x}Zn_{8+y}$ shows vacancies on two Au positions located on the OT and OH. For γ-$Au_{5-x}Zn_{8+y}$, the vacancy concentration increases with increasing Zn content. This kind of trend is generally observed in many γ-brass type structures that frequently occur for binary and ternary systems where the vacancy concentration increases as *vec* increases. Based on the refined compositions, the γ-type Mn–Al phases have a *vec*

range of 1.54–1.90 (including only *s* and *p* electrons, no *d* e⁻) for the Mn-rich and Al-rich phase boundaries, respectively. The upper *vec* boundary for the Al-rich region is significantly larger than that observed for γ-$Au_{5-x}Zn_{8+y}$ but is comparable to the value observed for γ-Cr_5Al_8 [51]. According to Pearson, rhombohedrally distorted γ-brass type phases could be stabilized by lowering its band structure energy, which occurs for phases with *vec* values higher than those for cubic γ-brasses [53]. In addition, the stability of γ-Ag_5Li_8 (*vec* = 1) has been rationalized in terms of lowering the band-structure energy by forming heavily populated bonding states near the bottom of the Ag-4*d* band [55]. According to the authors, the structural stability γ-Ag_5Li_8 does not follow a typical Hume-Rothery type mechanism, i.e. the formation of a pseudogap at the Fermi level in the electronic structure due to interactions between the Fermi surface and Brillouin zone planes [25].

Furthermore, an accurate determination of *vec* for γ-phases that involve transition metals from groups 6-10 remains open for discussion. According to the classical Hume-Rothery electron counting rule, only valence *s* and *p* electrons are included to calculate *vec*, which led to the *vec* range of 1.54–1.90 e^-/atom for the γ-Mn–Al series. However, from magnetic susceptibility measurements on Cr–Al and Mn–Al systems, the 3*d*-bands of Cr and Mn increasingly take 3*p* electrons from Al atoms with increasing Al concentration [56]. According to their report, Mn_5Al_8 and Cr_5Al_8 phases have 7.7 $d e^-$/Mn and 6.6 $d e^-$/Cr atom, respectively. If we assume a similar value of *d* e⁻ per Mn atom to calculate *vec* for the Al-rich composition, $Mn_{4.76}Al_{8.24}$, then *vec* is 1.64 [(24.69–3.33)/13] instead of 1.90. This possibly rationalizes why Al-rich γ-brass phases do not show any vacancies in their structures. In addition, they also reported 7.0 *d* e⁻/Mn and 6.3 *d* e⁻/Mn for Mn_6Al_7 and δ-Mn, respectively. The calculated *vec* for Mn-rich composition, $Mn_{6.32}Al_{6.68}$, is 1.541, with no contribution from *d* e^- from Mn atoms (7.0 *d* e⁻/Mn for Mn_6Al_8).

Magnetic behavior of $Mn_{4.92}Al_{8.08(2)}$

Magnetic behavior of $Mn_{4.92}Al_{8.08(2)}$ (loaded composition $Mn_{38}Al_{62}$) was examined using a cryogenic Quantum design MPMS in the temperature range of 2 K to 300 K. Figure 5 shows the measured Curie-Weiss plot and its magnetic susceptibility in the inset in a 1000 Oe applied field. For temperature above 70 K, the straight line behavior in χ^{-1}(T) suggests that $Mn_{4.92}Al_{8.08(2)}$ follows Curie-Weiss behavior with an estimated Curie-Weiss temperature of –190 K arrives from extrapolation of the linear portion of the χ^{-1}(T) curve. The corresponding effective moment of

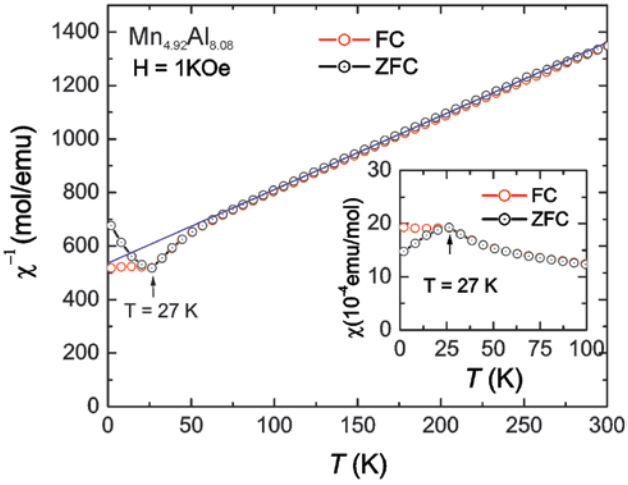

Fig. 5: Temperature-dependent, inverse magnetic susceptibility of a $Mn_{4.92}Al_{8.08(2)}$ sample. Inset: magnetic susceptibility in the temperature range from 2 K to 100 K.

the Mn atom in the sample, as estimated from the relation $\mu_{eff} = (8C/x)^{1/2}$ with Curie constant C and molar fraction Mn *x* is 2.88μ_B/Mn [57]. Below 70 K the susceptibility deviates from a simple Curie Weiss law and near 27 K manifests a broad feature with very clear zero-field-cooled and field-cooled hysteresis. These features are consistent with a spin-glass state for temperatures less than 27 K. Such a state is fully consistent with the disorder we have found in the site occupation as well as width of formation.

Electronic structure analysis

Calculations were performed on stoichiometric, rhombohedral γ-"Mn_5Al_8" as a representative composition of the title compound with the M2 site assigned to Mn and the M6 and M7 sites assigned to Al (crystal **I**). The decoration of atoms in the 26-atom γ-cluster is as follows: IT (3Mn + Al); OT (4Mn); OH (3Al + 3Mn); and CO (12 Al). The calculated DOS from LDA-based calculations yielded many sharp peaks at the Fermi level arising mainly from Mn 3*d* orbitals, with the major contribution from the OT sites. The Fermi level for γ-"Mn_5Al_8", corresponding to 118 e^-, falls on a peak which was analyzed as Mn–Mn antibonding interactions in the corresponding COHP curves (Figure 6c). This outcome in the non-spin polarized DOS curve suggests a potential electronic instability for γ-"Mn_5Al_8" that can be relieved through spin-polarization leading to some kind of magnetic ordering at low temperature. The calculated spin-polarized DOS and COHP curves from LDA are shown in Figure 6a. Also, the calculated total electronic energy was 29.63 *me*V/atom lower using LSDA than LDA.

As a result of the LSDA calculation, the Fermi level no longer resides on a peak of the DOS; rather, it falls into a pseudogap region. The temperature dependent magnetic susceptibility measurement down to 2 K on a sample $Mn_{4.92}Al_{8.08(2)}$ suggests a spin-glass state for temperatures below 27 K.

The calculated Fermi level from LSDA for γ-"Mn_5Al_8", as indicated by solid line in Figure 6a, falls in a pseudogap of the DOS. The partial DOS of Mn 3*d* orbitals shows a very broad band extending ca. 5 eV below the Fermi level, indicating strong interactions with Al 3*p* orbitals. In addition, the Mn 3*d* DOS shows small exchange splitting. The valence *s* and *p* orbitals of Mn and Al show nearly free-electron-like parabolic bands. The pseudogap at the Fermi level is a signature of γ-brasses and related Hume-Rothery phases, and is also observed for numerous quasicrystal approximant structures [18, 19, 58–62]. Assuming a rigid band model for γ-$Mn_{5+x}Al_{8-x}$, the calculated Fermi levels for Al-rich ($Mn_{4.76}Al_{8.24}$) and Mn-rich ($Mn_{6.32}Al_{6.68}$) compositions correspond to 116.08 e^- and 128.56 e^-, respectively, and they fall into the pseudogap (Figure 6a).

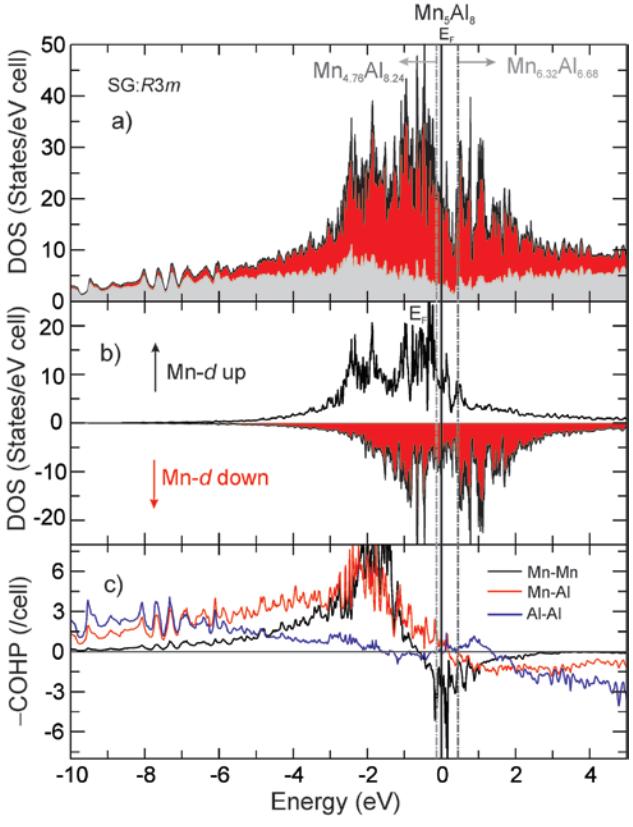

Fig. 6: Total DOS (a) and partial Mn-*d* DOS (b) curves for γ-"Mn_5Al_8" in LSDA. The contributions from Mn and Al are shown in red and grey, respectively. (c) COHP curves form LDA for Mn–Mn, Mn–Al and Al–Al interactions.

Figure 6c shows the calculated COHP curves for different pairwise Mn–Mn, Mn–Al and Al–Al interactions for "Mn_5Al_8" from LDA calculations. According to these curves, Mn–Al and Al–Al interactions are optimized at the Fermi level i.e. bonding orbitals are filled and anti-bonding orbitals are empty, and also lie within the pseudogap region of the DOS. On the other hand, Mn–Mn contacts show antibonding interactions at the Fermi level originating from IT–IT, IT–OT and OT–OH interactions, to suggest an electronic instability that can be alleviated by magnetic ordering. Similar electronic structures have also been calculated for rhombohedrally distorted γ-*T*Ga (*T* = Cr, Mn and Fe) phases and they show weak magnetic exchange interactions [29]. In addition, over the experimentally observed homogeneity range, the Mn–Al and Al–Al interactions show weakly bonding/non-bonding interactions.

Summary

Single crystals of the γ-phase $Mn_{5-x}Al_{8+x}$ ($-2 \le x \le 1$) were successfully grown using a Sn-flux, without incorporation of Sn into the structure according to EDS analysis and refinements from single crystal diffraction. γ-$Mn_{5-x}Al_{8+x}$ adopts the γ-Cr_5Al_8-type structure, which is a rhombohedral distortion of cubic γ-brass structures, with a phase width of 51.4–63.4 at.% Al at 650 °C. From the refined compositions, the observed *vec* range was estimated to be 1.643 (Al-rich) and 1.541 (Al-poor) e^-/a. The phase width of γ-$Mn_{5-x}Al_{8+x}$ arises from successive increase of Mn content on the IT and CO sites of the 26-atom γ-cluster, whereas the OT site is fully occupied by Mn and the OH site shows negligible variation from 50:50 mixtures of Mn:Al for all the refined compositions. The assigned homogeneity range from our studies agrees well with the report by Ellner. Electronic structure calculations for an idealized γ-"Mn_5Al_8" model shows that the Fermi level falls on a peak in the nonmagnetic (LDA) DOS, originating from Mn–Mn antibonding IT–IT, IT–OT and OT–OH interactions. However, upon spin polarized (LSDA) calculations, the Fermi level moves into a pseudogap, which is typically observed for Hume-Rothery phases. Magnetic measurements on a single phase γ-$Mn_{4.92}Al_{8.08(2)}$ suggest a spin-glass state for temperatures below 27 K.

Acknowledgements: S.T., Z.T., P.C.C. and G.J.M., were supported by the U.S. Department of Energy, Office of Basic Energy Sciences, Division of Materials Sciences and Engineering. T.N.L. was supported by the Critical Materials Institute, an Energy Innovation Hub funded by the U.S.

Department of Energy, Office of Energy Efficiency and Renewable Energy, Advanced Manufacturing Office. This work was carried out at the Ames Laboratory, which is operated for the U.S. Department of Energy by Iowa State University under Contract No. DE-AC02-07CH11358.

References

[1] S. Samson, *Nature* **1962**, *195*, 259.
[2] S. Samson, *Acta Crystallogr.* **1965**, *19*, 401.
[3] D. C. Fredrickson, S. Lee, R. Hoffmann, *Angew. Chem. Int. Ed.* **2007**, *46*, 1958.
[4] M. Conrad, B. Harbrecht, T. Weber, D. Y. Jung, W. Steurer, *Acta Crystallogr. B* **2009**, *B65*, 318.
[5] T. Weber, J. Dshemuchadse, M. Kobas, M. Conrad, B. Harbrecht, W. Steurer, *Acta Crystallogr. B* **2009**, *B65*, 308.
[6] J. Dshemuchadse, D. Y. Jung, W. Steurer, *Acta Crystallogr B* **2011**, *B67*, 269.
[7] K. Kovnir, M. Shatruk, *Eur. J. Inorg. Chem.* **2011**, *2011*, 3955.
[8] F. Stein, M. Palm, G. Sauthoff, *Intermetallics* **2004**, *12*, 713.
[9] F. Stein, M. Palm, G. Sauthoff, *Intermetallics* **2005**, *13*, 1056.
[10] A. Ormeci, A. Simon, Y. Grin, *Angew. Chem. Int. Ed.* **2010**, *49*, 8997.
[11] A. Simon, *Angew.Chem. Int. Ed.* **1983**, *22*, 95.
[12] R. L. Johnston, R. Hoffmann, *Z. Anorg. Allg. Chem.* **1992**, *616*, 105.
[13] T. F. Faessler and Editor, *Zintl Phases: Principles and Recent Developments. [In: Struct. Bonding (Berlin, Ger.), 2011; 139]*, Springer-Verlag, Berlin, Heidelberg, p. 1–161, **2011**.
[14] S. M. Kauzlarich and Editor, *Chemistry, Structure, and Bonding of Zintl Phases and Ions*. VCH Publishers, Inc., New York, p. 1–306, **1996**.
[15] H. Schäfer, B. Eisenmann, W. Müller, *Angew.Chem. Int. Ed.* **1973**, *12*, 694.
[16] U. Mizutani, *The Hume-Rothery rules for structurally complex alloy phases*. CRC Press, Taylor & Francis Group, Boca Raton, FL, p. 1–324, **2010**.
[17] S. Thimmaiah, N. A. Crumpton, G. J. Miller, *Z. Anorg. Allg. Chem.* **2011**, *637*, 1992.
[18] S. Thimmaiah, G. J. Miller, *Chem. Eur. J.* **2010**, *16*, 5461.
[19] S. Thimmaiah, G. J. Miller, *Inorg. Chem.* **2013**, *52*, 1328.
[20] W. Hornfeck, S. Thimmaiah, S. Lee, B. Harbrecht, *Chem. Eur. J.* **2004**, *10*, 4616.
[21] S. Thimmaiah, K. W. Richter, S. Lee, B. Harbrecht, *Solid State Sci.* **2003**, *5*, 1309.
[22] U. Mizutani, M. Inukai, H. Sato, E. S. Zijlstra, Q. Lin, *Phil. Mag.* **2014**, *94*, 2571.
[23] A.-P. Tsai, *Chem. Soc. Rev.* **2013**, *42*, 5352.
[24] T. Takeuchi, H. Sato, U. Mizutani, *J. Alloys Compd.* **2002**, *342*, 355.
[25] A. T. Paxton, M. Methfessel, D. G. Pettifor, *Proc. R. Soc. London Ser. A* **1997**, *453*, 1493.
[26] W. Xie, J. Liu, V. Pecharsky, G. J. Miller, *Z. Anorg. Allg. Chem.* **2015**, *641*, 270.
[27] W. Xie, G. J. Miller, *Chem. Mater.* **2014**, *26*, 2624.
[28] O. Gourdon, G. J. Miller, *Chem. Mater.* **2006**, *18*, 1848.
[29] O. Gourdon, S. L. Bud'ko, D. Williams, G. J. Miller, *Inorg. Chem.* **2004**, *43*, 3210.
[30] S. Thimmaiah, G. J. Miller, *Acta Cryst.* **2010**, *E66*, i5.
[31] M. Ellner, *Metall. Mater. Trans. A* **1990**, *21*, 1669.
[32] R. W. Schonover, G. P. Mohanty, *Mater. Sci. Eng.* **1969**, *4*, 243.
[33] T. Goedecke, W. Koester, *Z. Metallk.* **1971**, *62*, 727.
[34] *WinXPOW, V 3.0.2.1*, *Vol.* STOE & Cie GmbH, Germany, **2011**.
[35] APEX2 in *APEX2*, *Vol.* Bruker AXS Inc., Madison, Wisconsin, USA, **2013**.
[36] SHELXTLv2016 in *Vol.* Bruker AXS Inc., Madison, Wisconsin, USA, **2016**.
[37] O. K. Andersen, *Phys. Rev.* **1975**, *B12*, 3060.
[38] O. K. Andersen, *Phys. Rev.* **1986**, *B34*, 2439.
[39] O. K. Andersen, O. Jepsen, *Phys. Rev. Lett.* **1984**, *53*, 2571.
[40] O. K. Andersen, O. Jepsen, D. Glötzel, in *Highlights of Condensed Matter Theory* (Eds. F. Bassani, F. Fumi and M. P. Tosi) North-Holland, New York, p. 59, **1985**.
[41] R. Dronskowski, P. E. Bloechl, *J. Phys. Chem.* **1993**, *97*, 8617.
[42] U. Von Barth, L. Hedin, *J. Phys. C* **1972**, *5*, 1629.
[43] D. D. Koelling, B. N. Harmon, *J. Phys. C* **1977**, *10*, 3107.
[44] O. Jepsen, O. K. Andersen, *Z. Phys. B* **1995**, *97*, 35.
[45] P. E. Blöchl, O. Jepsen, O. K. Andersen, *Phys. Rev.* **1994**, *B49*, 16223.
[46] A. Kontio, E. D. Stevens, P. Coppens, R. D. Brown, A. E. Dwight, J. M. Williams, *Acta Cryst.* **1980**, *B36*, 435.
[47] Z. W. Liu, C. Chen, Z. G. Zheng, B. H. Tan, R. V. Ramanujan, *J. Mater. Sci.* **2012**, *47*, 2333.
[48] H. Fang, J. Cedervall, F. J. M. Casado, Z. Matej, J. Bednarcik, J. Ångström, P. Berastegui, M. Sahlberg, *J. Alloys Compd.* **2017**, *692*, 198.
[49] J. H. Park, Y. K. Hong, S. Bae, J. J. Lee, J. Jalli, G. S. Abo, N. Neveu, S. G. Kim, C. J. Choi, J. G. Lee, *J. Appl. Phys.* **2010**, *107*, 09A731.
[50] L. Pauling, B. Kamb, *Proc. Natl. Acad. Sci. U. S. A.* **1986**, *83*, 3569.
[51] M. Ellner, J. Braun, B. Predel, *Z. Metallkd.* **1989**, *80*, 374.
[52] T. Lindahl, S. Westman, *Acta Chem. Scand.* **1969**, *23*, 1181.
[53] J. K. Brandon, W. B. Pearson, P. W. Riley, C. Chieh, R. Stokhuyzen, *Acta Cryst.* **1977**, *B33*, 1088.
[54] F. Stein, S. C. Vogel, M. Eumann, M. Palm, *Intermetallics* **2010**, *18*, 150.
[55] U. Mizutani, R. Asahi, H. Sato, T. Noritake, T. Takeuchi, *J. Phys. Condens. Matter.* **2008**, *20*, 275228.
[56] W. Koester, E. Wachtel, K. Grube, *Z. Metallkd.* **1963**, *54*, 393.
[57] F. Jimenez-Villacorta, J. L. Marion, T. Sepehrifar, M. Daniil, M. A. Willard, L. H. Lewis, *Appl. Phys. Lett.* **2012**, *100*, 112408/1.
[58] Q. Lin, J. D. Corbett, *J. Am. Chem. Soc.* **2007**, *129*, 6789.
[59] Q. Lin, J. D. Corbett, *Inorg. Chem.* **2008**, *47*, 7651.
[60] Q. Lin, J. D. Corbett, *Inorg. Chem.* **2010**, *49*, 10436.
[61] H. Ko, O. Gourdon, D. Gout, E.-D. Mun, S. Thimmaiah, G. J. Miller, *Inorg. Chem.* **2010**, *49*, 11505.
[62] O. Gourdon, D. Gout, D. J. Williams, T. Proffen, S. Hobbs, G. J. Miller, *Inorg. Chem.* **2006**, *46*, 251.

Supplemental Material: The online version of this article (DOI: 10.1515/zkri-2017-0003) offers supplementary material, available to authorized users.